JOURNAL OF THERMOPHYSICS AND HEAT TRANSFER
Vol. 7, No. 3, July–Sept. 1993

Radiative Transfer by the YIX Method in Nonhomogeneous, Scattering, and Nongray Media

Pei-feng Hsu,* Zhiqiang Tan,† and John R. Howell‡
University of Texas at Austin, Austin, Texas 78712

A numerical solution of the integral equation of radiative heat transfer using the YIX method involving a mixture of highly anisotropic scattering particles and a nongray absorbing gas is presented. To validate the three-dimensional calculation, bench mark solutions are established on a model problem using a high-order accuracy method, the product integration method (PIM). Various effects, e.g., the discrete ordinates sets, first integration point of the YIX quadrature, optical thickness of the medium, grid sizes, and spectral resolution on the accuracy of the three-dimensional calculation are discussed. Results for three-dimensional calculations are presented. For all cases, the pressure variation has less significant effect on the results than those by particle density or temperature variations. The three-dimensional nonhomogeneous cases have different trends of variation in radiative flux and divergence due to their nonuniform particle density distribution and nonisothermal participating medium. The use of the YIX method with discrete ordinates for the multidimensional calculations of highly anisotropic scattering and spectrally-dependent medium is shown to be accurate and flexible.

Nomenclature

A = area, m^2
a = absorption coefficient, m^{-1}; band symmetry factor, Eq. (9)
a_n = coefficient of scattering phase function, Eq. (2)
b_n = coefficient of scattering phase function, Eq. (3)
D = particle diameter, μm
E_n = exponential integral of order n
e = emissive power of the medium, W/m^2
f = coefficient of scattering phase function, Eq. (6)
g = coefficient of scattering phase function, Eq. (6)
i = radiation intensity, W/m^2
K = kernel of integral equation, Eq. (14)
L = distance between boundaries, m
N = particle density, m^{-3}
$\mathbf{n}$ = inward unit normal vector
P = radiation pressure, J/m^3/sr
P_e = broadening pressure parameter of absorbing gas
P_n = Legendre function of order n
$\mathbf{q}_r$ = radiative heat flux, W/m^2
R = radiation quantity
$R(r, \omega_i)$ = distance from a point within the medium to the wall in the direction ω_i, Eq. (16)
$\mathbf{r}$ = position vector
S_c = mean line intensity, m^2/cm/g, Eq. (10)
S_k = expansion function of Legendre series
s = scattering coefficient, m^{-1}
T = temperature, K
V = volume, m^3
W_i = weights of discrete ordinates set
w = radiative heat flux, W/m^2
w_i = level weights of discrete ordinates set
x = distance, m
α = band intensity, m^2/cm/g, Eq. (10)
β = coefficient of anisotropic scattering phase function; mean linewidth-spacing parameter
δ = Dirac-delta function; absorption line spacing, cm^{-1}
ε = surface emissivity
η = direction cosine; wave number, cm^{-1}
κ = extinction coefficient, m^{-1}
λ = wavelength, μm
μ = direction cosine
ξ = direction cosine
ρ = density of the gaseous mixture, kg/m^3
σ = Stefan-Boltzmann constant, $5.6696 \cdot 10^{-8}$ W/m^{2}K^4
τ = local optical thickness
Φ = normalized scattering phase function
Ω = domain or boundary of integration, Eqs. (11–13)
ω = scattering albedo; bandwidth parameter, cm^{-1}; solid angle
$\boldsymbol{\omega}$ = unit vector, Eq. (15)

Subscripts
b = blackbody
g = participating medium for radiative transfer
r = radiation
s = boundary surface
λ = wavelength

Superscript
$'$ = incident direction; indicates effective scattering coefficient

Introduction

RADIATIVE heat transfer in an absorbing, emitting, and scattering particulate/gas mixture is a problem of practical importance, e.g., in the design of industrial furnaces, and many combustion devices. A solution method that is accurate, efficient with both computing time and storage, flexible with complex geometry, and allows incorporation of real gas properties is needed for the prediction of the radiative performance. Few methods currently exist that can satisfy all or part of the requirements. The Monte Carlo method is flexible and requires little storage, but may be extremely time consuming and the results are subject to statistical error. The zonal method and finite element method are accurate, but

---

Received April 30, 1992; revision received Aug. 17, 1992; accepted for publication Aug. 18, 1992. Copyright © 1993 by the authors. Published by the American Institute of Aeronautics and Astronautics, Inc., with permission.

*Postdoctoral Fellow, Mechanical Engineering Department.

†Postdoctoral Fellow, Aerospace Engineering and Engineering Mechanics Department.

‡Baker-Hughes Professor, Mechanical Engineering Department. Associate Fellow AIAA.

time and storage consuming. It is also difficult to handle a nonhomogeneous or anisotropically scattering medium using the zonal method. The product integration method,[1] while faster than the zonal method and finite element method, does not reduce the required storage. The "discrete ordinates" method, developed to solve neutron transport problems, though accurate and requiring less memory as compared to the other methods (except the Monte Carlo) for large grid systems, suffers from ray effects[2] and large computer time for multidimensional combined mode heat transfer problems.

In this article, a recently developed numerical YIX method[3] is used to solve an example radiative transfer problem simulating a combustion chamber filled with different concentrations of highly anisotropically scattering particles and an absorbing gas under different pressures. Results are presented for the three-dimensional homogeneous and nonhomogeneous spectral-dependent participating medium. The solution procedure and effect of various quadratures on the solution for a multidimensional geometry is described in detail.

Mathematical Formulation

Phase Functions

The radiative heat transfer equation is written as[4]

$$\frac{\mathrm{d}i(r,\omega)}{\mathrm{d}l} = -\kappa i(r,\omega) + a i_b(r) + \frac{s}{4\pi}\int_{\omega'=4\pi} i(r,\omega') \cdot \Phi(\omega,\omega')\,\mathrm{d}\omega' \tag{1}$$

where the phase function, based on the Mie theory, can be expressed as[5]

$$\Phi(\omega,\omega') = \sum_{n=0}^{N} (2n+1) a_n P_n(\omega\cdot\omega') \tag{2}$$

For particles with size parameter $\pi D/\lambda$ much greater than unity, the scattering phase function is characterized by a strong forward spike. To represent the sharp spike in the context of Eq. (2) requires at least 50 terms. For engineering calculation, this is impractical. One remedy is to use the Dirac-delta function to approximate the forward spike.[6,7] Hence, Eq. (2) can be rewritten as

$$\Phi_d(\omega,\omega') = 2f\delta(\omega'-\omega) + (1-f) \cdot \sum_{n=0}^{M} (2n+1) b_n P_n(\omega\cdot\omega') \tag{3}$$

where

$$\delta(\omega'-\omega) = \begin{cases} \infty, \text{ if } \omega = \omega' \\ 0, \text{ if } \omega \neq \omega' \end{cases}, \quad \omega \in (0, 4\pi) \tag{4}$$

$$\frac{1}{4\pi}\int \delta(\omega'-\omega) i(r,\omega')\,\mathrm{d}\omega' = \frac{i(r,\omega)}{2} \tag{5}$$

This form is known as the delta-Eddington formulation. It is noted that although the Dirac-delta function provides a good approximation to the forward spiked phase function as well as mathematical convenience, Eq. (3) is not a smooth phase function.

The problem of interest consists of a mixture of highly anisotropically scattering carbon particles with phase function expressed in the form of Eq. (3) in a known gas mixture of CO_2 and N_2. The CO_2 mole fraction is 0.21. The bounding surface is opaque and cold.

The phase function for carbon particles is given as

$$\Phi_d(\omega,\omega') = 2f\delta(\omega'-\omega) + (1-f)[1 + 3gP_1(\omega\cdot\omega')] \tag{6}$$

with $f = 0.111$ and $g = 0.215$. The $P_n(\omega\cdot\omega')$ can be expanded using the addition theorem of the Legendre function,[8] and

$$\omega\cdot\omega' = \mu\mu' + \xi\xi' + \eta\eta' \tag{7}$$

where μ, ξ, η are the direction cosines of ω with respect to each coordinate axis. In three-dimensional geometry

$$P_1(\omega\cdot\omega') = \sum_{k=1}^{3} S_k(\omega) S_k(\omega')$$

where $S_k(\omega)$, $k = 1, 2, 3$ is the component of the direction cosines of ω. Similarly

$$P_2(\omega\cdot\omega') = \sum_{k=4}^{8} S_k(\omega) S_k(\omega')$$

where $S_k(\omega)$, $k = 4, \ldots, 8$ is the linear combination of the component of the unit radiation pressure tensor in the direction of ω. In the one-dimensional case

$$P_1(\omega\cdot\omega') = S_3(\omega)S_3(\omega') = \mu\mu'$$

$$P_2(\omega\cdot\omega') = S_4(\omega)S_4(\omega') = \tfrac{1}{2}(3\mu^2 - 1)\cdot\tfrac{1}{2}(3\mu'^2 - 1)$$

and the $S_4(\omega)$ is exactly the Rayleigh scattering phase function for small particles. After the $P_n(\omega\cdot\omega')$ terms are expanded, the phase function can be expressed as

$$\Phi(\omega,\omega') = \sum_{n=0}^{N} (2n+1) a_n P_n(\omega\cdot\omega') = \sum_{k=0}^{m} \beta_k S_k(\omega) S_k(\omega') \tag{8}$$

where $\beta_0 = 1$, $\beta_1 = \beta_2 = \beta_3 = 3a_1$, $\beta_4 = 5a_2/4$, $\beta_5 = \beta_6 = 5a_2/3$, $\beta_7 = \beta_8 = 5a_2/12$, etc.

With Eq. (3) substituted into Eq. (1) and performing the integration with the Dirac-delta function, Eq. (1) becomes

$$\frac{\mathrm{d}i(r,\omega)}{\mathrm{d}l} = -(a + s - fs) i(r,\omega) + a i_b(r) + \frac{s(1-f)}{4\pi} \cdot \int_{\omega'=4\pi} i(r,\omega') \sum_{n=0}^{M} (2n+1) b_n P_n(\omega\cdot\omega')\,\mathrm{d}\omega' \tag{9}$$

Let $s' = (1-f)s$, and define s' as the effective scattering coefficient, and the above equation is exactly the same as Eq. (1).

Carbon Dioxide Gas Absorption

For an absorbing gas, the exponential wide band model by Edwards[9,10] is used to compute the spectral absorption coefficient, which is given by

$$a_\eta = \rho \frac{S_c}{\delta} \frac{\sinh(\pi\beta/2)}{\cosh(\pi\beta/2) - \cos[2\pi(\eta - \eta_c)/\delta]} \tag{10}$$

where

$$(S_c/\delta) = (\alpha/\omega)\exp[-(\alpha/\omega)|\eta - \eta_c|]$$

$$\beta = (C_2^2 P_e/4C_1C_3)$$

$$\alpha = C_1$$

$$\omega = C_3$$

$$\delta = 30C_3(T = T_0)$$

where C_1, C_2, and C_3 are given in Ref. 4. Definitions of the parameters are listed in the Nomenclature and also in a detailed review by Edwards.[10] Figure 1 shows the spectral variation of the total absorption coefficient of the particle/gas mixture at 1000 K, 1 atm total pressure, and carbon particle density of $2 \cdot 10^7$ m^{-3}.

Integral Solution for Radiative Transfer Equation

The integral formulation of the radiative heat transfer in a general three-dimensional, gray, emitting, absorbing, and anisotropic scattering media corresponding to Eq. (1) by Tan[1] is used here:

$$\begin{aligned}4e_g(\boldsymbol{r}) - \frac{1}{a}\nabla\cdot\mathbf{q}_r(\boldsymbol{r}) = \int\int\int_\Omega K(\boldsymbol{r}, \boldsymbol{r}')\Bigg[\kappa e_g(\boldsymbol{r}')\\ - \frac{s}{4a}\nabla\cdot\mathbf{q}_r(\boldsymbol{r}')\Bigg]\,\mathrm{d}V(\boldsymbol{r}') + \frac{s}{4}\sum_{k=1}^{M}\beta_k\int\int\int_\Omega K(\boldsymbol{r}, \boldsymbol{r}')w_k(\boldsymbol{r}')\\ \cdot S_k(\omega)\,\mathrm{d}V(\boldsymbol{r}') + \int\int_{\partial\Omega} K(\boldsymbol{r}, \boldsymbol{r}')\Bigg[e_s(\boldsymbol{r}')\\ - \frac{1-\varepsilon}{\varepsilon}q_s(\boldsymbol{r}')\Bigg]\cos(\boldsymbol{r} - \boldsymbol{r}', \boldsymbol{n}')\,\mathrm{d}A(\boldsymbol{r}') \qquad \boldsymbol{r}\in\Omega\end{aligned} \tag{11}$$

$$\begin{aligned}w_i(\boldsymbol{r}) = \int\int\int_\Omega K(\boldsymbol{r}, \boldsymbol{r}')\Bigg[\kappa e_g(\boldsymbol{r}') - \frac{s}{4a}\nabla\cdot\mathbf{q}_r(\boldsymbol{r}')\Bigg]\\ \cdot S_i(\omega)\,\mathrm{d}V(\boldsymbol{r}') + \frac{s}{4}\sum_{k=1}^{M}\beta_k\int\int\int_\Omega K(\boldsymbol{r}, \boldsymbol{r}')w_k(\boldsymbol{r}')S_k(\omega)\\ \cdot S_i(\omega)\,\mathrm{d}V(\boldsymbol{r}') + \int\int_{\partial\Omega} K(\boldsymbol{r}, \boldsymbol{r}')\Bigg[e_s(\boldsymbol{r}') - \frac{1-\varepsilon}{\varepsilon}q_s(\boldsymbol{r}')\Bigg]\\ \cdot S_i(\omega)\cos(\boldsymbol{r} - \boldsymbol{r}', \boldsymbol{n}')\,\mathrm{d}A(\boldsymbol{r}') \qquad i = 1, 2, \ldots, M \qquad \boldsymbol{r}\in\Omega\end{aligned} \tag{12}$$

$$\begin{aligned}e_s(\boldsymbol{r}) - \frac{1}{\varepsilon}q_s(\boldsymbol{r}) = \int\int\int_\Omega K(\boldsymbol{r}, \boldsymbol{r}')\Bigg[\kappa e_g(\boldsymbol{r}') - \frac{s}{4a}\nabla\cdot\mathbf{q}_r(\boldsymbol{r}')\Bigg]\\ \cdot\cos(\boldsymbol{r}' - \boldsymbol{r}, \boldsymbol{n})\,\mathrm{d}V(\boldsymbol{r}') + \frac{s}{4}\sum_{k=1}^{M}\beta_k\int\int\int_\Omega K(\boldsymbol{r}, \boldsymbol{r}')w_k(\boldsymbol{r}')\\ \cdot S_k(\omega)\cos(\boldsymbol{r}' - \boldsymbol{r}, \boldsymbol{n})\,\mathrm{d}V(\boldsymbol{r}') + \int\int_{\partial\Omega} K(\boldsymbol{r}, \boldsymbol{r}')\Bigg[e_s(\boldsymbol{r}')\\ - \frac{1-\varepsilon}{\varepsilon}q_s(\boldsymbol{r}')\Bigg]\cos(\boldsymbol{r} - \boldsymbol{r}', \boldsymbol{n}')\cos(\boldsymbol{r}' - \boldsymbol{r}, \boldsymbol{n})\,\mathrm{d}A(\boldsymbol{r}')\\ \boldsymbol{r}\in\partial\Omega\end{aligned} \tag{13}$$

In the above equations, e_g and e_s are the blackbody emissive powers of the medium and the boundary, q_s is the net radiative heat flux on the wall, and s is s' if the delta-Eddington phase function is used [Eq. (9)]. The kernel K is

$$K(\boldsymbol{r}, \boldsymbol{r}') = \Bigg[\exp\left(-\int_0^{|\boldsymbol{r}-\boldsymbol{r}'|}\kappa(\boldsymbol{r} + \omega t)\,\mathrm{d}t\right)\Bigg/(\pi|\boldsymbol{r} - \boldsymbol{r}'|^2)\Bigg] \tag{14}$$

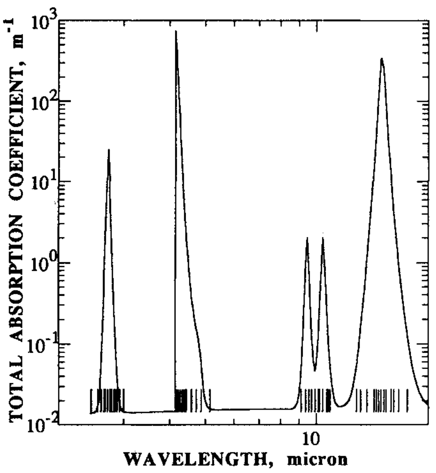

Fig. 1 Total spectral absorption coefficient of carbon particles plus gas mixture. Total pressure 1 atm and particle concentration $2 \cdot 10^7$ m^{-3}. The short vertical lines indicate the points (55) used in the spectral integration.

and the unit vector

$$\boldsymbol{\omega} = [(\boldsymbol{r} - \boldsymbol{r}')/(|\boldsymbol{r} - \boldsymbol{r}'|)] \tag{15}$$

When the medium is nongray, the integral equations are essentially the same, except that all radiative quantities are wavelength-dependent, and e_g and e_s are replaced by the Planck function.

Numerical Method

The integrations of Eqs. (11–13) are performed using the YIX method.[3] The integral equations are first rewritten into the distance-angular form. The YIX method constructs and prestores the numerical integral quadrature ordinates for the distance integral with different kernel function. The name YIX reflects the spatial distribution pattern of ordinate positions in three, two, or four ordinate directions in two dimensional problems. The integration is basically an equal weight, fixed ordinates (in optical thickness coordinate for each kernel function) quadrature as opposed to the other nonequal weights quadratures, e.g., the Gaussian quadrature. The advantage of the YIX method is eliminating the time-consuming evaluation of the kernels (i.e., exponential integrals in one dimension, Bickley's functions in two dimensions, and exponential functions in three dimensions) in the distance integrals. In addition, it is especially suitable for a nonhomogeneous medium since the effort to generate the integration points and perform integrations is the same as for a homogeneous medium. To maintain the same order of accuracy in angular integration at volume and boundary elements in three-dimensional geometries, the fully symmetric discrete ordinates and weights sets proposed in Ref. 11 were used. The angular quadrature sets are constructed to be invariant under any 90-deg rotation about an axis, and also satisfy certain order of moment integrations of intensity over the sphere (full range) and hemisphere (half-range). The use of discrete ordinates sets will be discussed later.

The difficulties involved in a multidimensional geometry are 1) to locate in which volume element the integration point lies; and 2) to determine which boundary element j is struck by the beam originating from volume element i. For a regular geometry as in the present study, the problems are easy to handle. For an irregular or nonconcave shape, extra care is needed to efficiently locate the integration points and identify the struck boundary element.

The volume and surface integrations on the right sides of Eqs. (11–13) are constructed as follows:

$$\iiint_{\Omega} K(\boldsymbol{r}, \boldsymbol{r}')F(\boldsymbol{r}')\,\mathrm{d}V(\boldsymbol{r}') = \int_{4\pi} \frac{\mathrm{d}\omega}{\pi} \int_0^{R(r,\omega)} \exp\left[-\int_0^t \kappa(\boldsymbol{r} + \omega t')\,\mathrm{d}t'\right] F(\boldsymbol{r} + \omega t)\,\mathrm{d}t \approx \sum_i^{N_W^*} W_i \int_0^{R(r,\omega)} \exp\left[-\int_0^t \kappa(\boldsymbol{r} + \omega_i t')\,\mathrm{d}t'\right] F(\boldsymbol{r} + \omega_i t)\,\mathrm{d}t \tag{16}$$

$$\iint_{\partial\Omega} K(\boldsymbol{r}, \boldsymbol{r}')F(\boldsymbol{r}')\cos(\boldsymbol{r} - \boldsymbol{r}', \boldsymbol{n})\,\mathrm{d}A(\boldsymbol{r}') = \int_0^{4\pi} \exp\left[-\int_0^t \kappa(\boldsymbol{r} + \omega t')\,\mathrm{d}t'\right] F(r + \omega R)\frac{\mathrm{d}\omega}{\pi} \approx \sum_i^{N_W^*} W_i \exp\left[-\int_0^t \kappa(r + \omega_i t')\,\mathrm{d}t'\right] F(\boldsymbol{r} + \omega_i R)$$

$$N_W^* = N_W, \quad \text{if} \quad \boldsymbol{r} \in \Omega$$

or

$$N_W^* = N_W/2, \quad \text{if} \quad \boldsymbol{r} \in \partial\Omega \tag{17}$$

where $R(\boldsymbol{r}, \omega)$ is defined as

$$R(\boldsymbol{r}, \omega) = \min_{r+\omega t, t>0} |\boldsymbol{r} + \omega t|$$

and equals the length of a beam emitted from $\boldsymbol{r}$ in ω direction and striking the nearest boundary.

The N_W is the number of ordinates, which depends on the order of discrete ordinates set used. For the *Sn* discrete ordinates set, $N_W = n(n + 2)$. The distance integrals in Eq. (16) are evaluated using the YIX quadrature. A schematic of the double integration is shown in Fig. 2. It is interesting to note that the right sides of Eqs. (11) and (12) are essentially the same except for the additional S_i term in Eq. (12). Therefore, the integrations in Eq. (12) can be avoided and a significant reduction of computational time can be achieved. Additionally, the current scheme has the flexibility to use multiple discrete ordinates sets in the formulation, which is very advantageous in dealing with the ray effect. The ray effect is caused when variations in boundary temperature or fluxes occur within a given ordinate direction where the boundary conditions are assumed to be constant. The resulting error is most serious in the optically thin region and can be alleviated with a higher order *Sn* set. However, in an optically thick region where the ray effect is less evident, a lower order of *Sn* set could be used to reduce computational time. This flexibility does not exist in the conventional discrete ordinates method[11,12] for the differential-integral formulation of radiative transfer equation, where a consistent discrete ordinates set has to be used even in the homogeneous case.

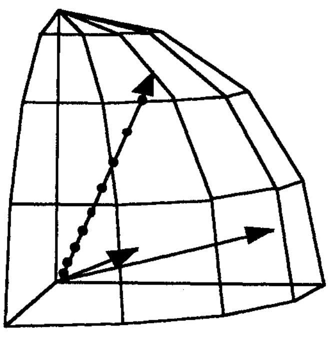

Fig. 2 Schematic of three-dimensional YIX integration at one node. Example of S4 discrete ordinates set in one octant is shown. The round dots on one of the directions indicates the integration points.

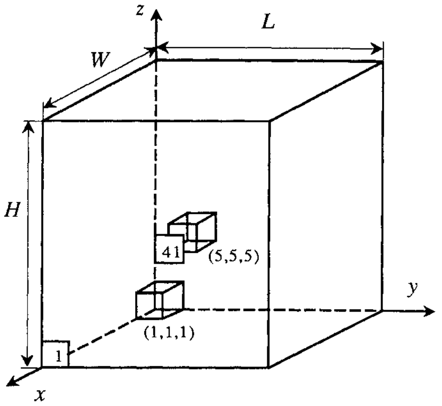

Fig. 3 Geometry of the bench mark problem and model problems. Note that in the model problems the coordinate origin lies in the center of the rectangular enclosure, and W = 2 m, H = 3 m, L = 5 or 8 m.

Solution Procedure

The discretized integrals of Eqs. (11–13) are solved by iteration. The algorithm is 1) give an initial guess for $\nabla\cdot\mathbf{q}_{r,\lambda}$, $w_{k,\lambda}(r)$, and $q_{s,\lambda}(r)$, with $e_{g,\lambda}(r)$, $e_{s,\lambda}(r)$ known; 2) calculate integrals on the right side of Eqs. (11–13) by the YIX quadrature; 3) calculate the new $\nabla\cdot\mathbf{q}_{r,\lambda}$, $w_{k,\lambda}(r)$; 4) go to step 2 unless the convergence criterion is satisfied, and 5) steps 1–4 are performed for each wavelength of interest. Then spectral integration is performed to integrate the $\nabla\cdot\mathbf{q}_{r,\lambda}$, $w_{k,\lambda}(r)$, and $q_{s,\lambda}(r)$ from 1 to 20.408 μm using the trapezoidal method (or other more sophisticated scheme). The details of spectral integration will be discussed later.

Bench Mark Solutions of a Model Problem

To validate the three-dimensional code, it is necessary to compare with a bench mark solution. The product integration method (PIM) was used to solve the radiative transfer within a unit cube with gray participating medium for its high-order accuracy and time efficiency.[1,13] The cube has three adjacent hot black walls with $e_s = 1$ (dimensionless) on surfaces at $x = 0$, $y = 0$, and $z = 1$ (Fig. 3). The remaining three walls are cold ($e_s = 0$) and also black.[14] The medium is nonscattering and in radiative equilibrium. Table 1 shows the emissive power distribution at $y = z = 0.625$, which is solved by PIM. Different grids are used to determine the discretization error of the bench mark solution itself. As shown in the Table 1 for $\kappa = 1$, a 12 × 12 × 12 grid provides three-digits accuracy as compared with the 36 × 36 × 36 grid. It has been shown that the discretization error decays rapidly with the grid size in one-dimensional and two-dimensional calculations.[13] A similar trend can be seen for the three-dimensional geometry. The YIX calculations using a 12 × 12 × 12 grid are tabulated along with the PIM bench mark in Table 1. The error column shows the difference between YIX12 and PIM36 calculations.

Effect of Discrete Ordinates Sets

The discrete ordinates direction set and associated weights are obtained from Lathrop and Carlson.[15] As mentioned earlier, the fully symmetric ordinates set is required to ensure an invariant solution with respect to any coordinate system orientation in homogeneous or nonhomogeneous medium. All fully symmetric ordinates sets satisfy a full-range odd-moment integration (due to its symmetry property), i.e.

$$\int_{-1}^{1} \frac{\mu^{2j+1}}{2}\,\mathrm{d}\mu = 0 = \sum_{i=1}^{n} \mu_i^{2j+1} w_i$$

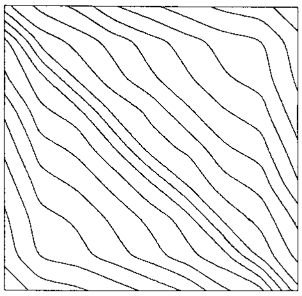

a) YIX method with S8 discrete ordinates

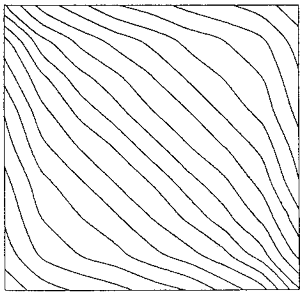

b) YIX method with S12 discrete ordinates

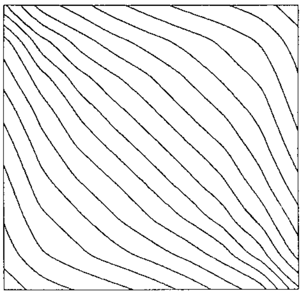

c) YIX method with S16 discrete ordinates

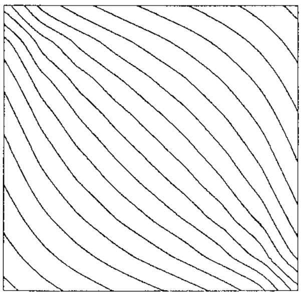

d) Results of PIM for 9 × 9 × 9 grid

Fig. 4 Emissive power contours of the bench mark problem. The left and lower edges of the plots near the hot walls and the right and upper edges near the cold walls.

for

$$j = 0, 1, \ldots, n/2 \tag{18}$$

where $\pm\mu_i$ are the abscissae on the axis between $[-1, 1]$. The level weight w_i is defined as

$$w_i = \pi \sum W_j(\mu_j = \mu_i, \xi_j, \eta_j)$$

An additional constraint can be imposed to generate the required discrete ordinates set, e.g., to satisfy half-range integration of all moments of $j = 0, 1, \ldots, n/2$

$$\int_0^1 \frac{\mu^j}{2}\,\mathrm{d}\mu = \frac{1}{j+1} = \sum_{i=1}^{n/2} \mu_i^j w_i \tag{19}$$

Table 1 Comparison of emissive power by the PIM and YIX method on the bench mark problem

x, m	PIM 36	PIM 12	YIX 12	Error[a]
0.01389	0.76228			
0.04167	0.74022	0.73970	0.75180	1.6
0.06944	0.72004			
0.09722	0.70102			
0.12500	0.68293	0.68265	0.66794	−2.2
0.15278	0.66568			
0.18056	0.64924			
0.20833	0.63355	0.63339	0.63146	−0.3
0.23611	0.61858			
0.26389	0.60426			
0.29167	0.59055	0.59045	0.58843	−0.3
0.31944	0.57738			
0.34722	0.56469			
0.37500	0.55240	0.55235	0.54551	−1.2
0.40278	0.54045			
0.43056	0.52875			
0.45833	0.51725	0.51722	0.51520	−0.4
0.48611	0.50585			
0.51389	0.49449			
0.54167	0.48309	0.48310	0.48242	−0.1
0.56944	0.47158			
0.59722	0.45988			
0.62500	0.44793	0.44797	0.44202	−1.3
0.65278	0.43564			
0.68056	0.42294			
0.70833	0.40977	0.40985	0.40569	−1
0.73611	0.39606			
0.76389	0.38174			
0.79167	0.36676	0.36691	0.36500	−0.5
0.81944	0.35106			
0.84722	0.33461			
0.87500	0.31736	0.31762	0.32867	3.5
0.90278	0.29927			
0.93056	0.28023			
0.95833	0.26004	0.26053	0.24501	−6
0.98611	0.23795			

[a] The % error of YIX12 compared with PIM36.

The numbers in the column headings indicate the grid used, e.g., 36 represents a 36 × 36 × 36 grid. The YIX method uses S12 discrete ordinates set and first integration point of 0.01. The data shown are the emissive powers at $y = z = 0.625$ and various x locations.

Discrete ordinates sets Sn of $n = 4$, 6, and 8 to be used in conjunction with Eqs. (16) and (17) are listed in Refs. 12 and 15. However, using Eq. (19) for $n \geq 12$ will produce negative weights, which affects numerical stability and is therefore undesirable. An alternative is to satisfy half-range zeroth, second, and a special set of the first-moment quadratures (see detailed discussion in Ref. 15), which leads to apparently always positive weight sets. Some of these ordinates sets used here are S12 and S16.

Figure 4 shows the results on the bench mark problem using the different discrete ordinates sets. All calculations used a 9 × 9 × 9 grid and 0.01 as the first integration point for the YIX distance quadrature. The emissive power contour plots show the values at the x-y plane of $z = 0.5$ m in each case. Note that only the ranges of 1/18 m $\leq x, y \leq$ 17/18 m are shown. The bench mark solution is presented in Fig. 4d. It was found that for Sn with $n \leq 8$, the error was large. For the S12 discrete ordinates set, the maximum error occurs at nodes near walls, and is around 6% (see Table 1, with a 12 × 12 × 12 grid). Overall, the average error is about 1–2%. For S16, the maximum error is about 3%, and the average error is less than 1%. The CPU time, which is proportional to the number of ordinates used, increased by a factor of 1.7 from S12 to S16. For computational time consideration, S12 is used throughout this study since it achieves reasonable accuracy.

Ray Effects and Optical Thickness

The YIX scheme was tested further against the bench marks for accuracy at optically thin ($\kappa = 10^{-2}$ and 10^{-5}) and thick

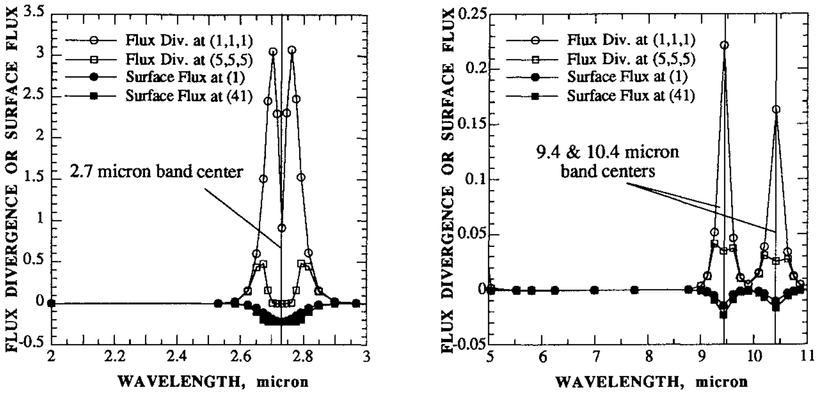

a) 2.7-μ Band

c) 9.4- and 10.4-μ Band

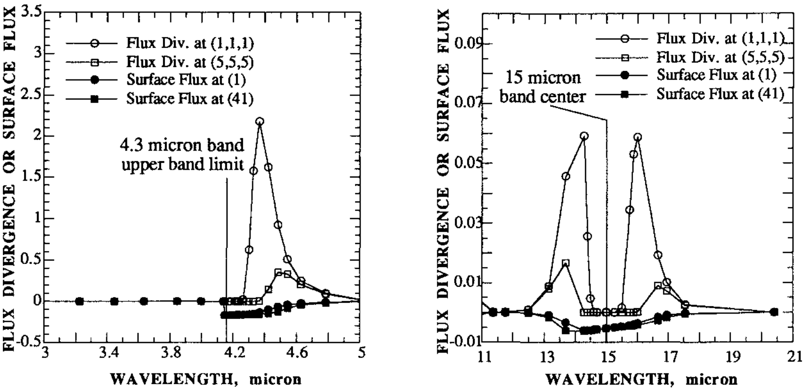

b) 4.3-μ Band

d) 15-μ Band

Fig. 5 Dimensionless divergence of radiative flux at a corner volume node (1, 1, 1) and center volume node (5, 5, 5) and surface flux at boundary nodes (1) and (41) in a 9 × 9 × 9 grid cubic geometry. The two volume nodes and two surface nodes are shown in Fig. 3. The problem involved 0.21 mole fraction of CO_2 at 1 atm in a cube with cold black walls at 1000 K. The surface flux and divergence are normalized with respect to the blackbody emissive power at 1000 K.

regions ($\kappa = 10$). The accuracy improved significantly using the same discrete ordinates set at higher optical thickness. This was due to the smaller influence of the ray effect from the boundary. It is concluded that at large optical thickness the use of a lower order of *Sn* set is justified. In fact, when optical thickness is very large, the radiation is an isotropic diffusion process. Therefore, only the variation in distance is important. It is expected that six angular directions will be sufficient at large optical thickness. Detailed quantification of this effect needs further study. On the other hand, at low optical thickness, use of S16 still deviated from the bench mark solution quite significantly, especially at the nodes near walls. For this particular bench mark problem, it was the ray effects that caused the error (see Ref. 2), especially near the walls where the effects were strongest. As mentioned previously, higher order discrete ordinate sets could be used in the nonhomogeneous medium with the YIX method in optically thin regions where the rays effect is expected. This also can be applied in the homogeneous medium at the optically thin spectral range. However, for the three-dimensional problems considered later in this article, cold walls are assumed, and the ray effect is not present.

Effect of the First YIX Integration Point in Three-Dimensional Quadrature

The input first integration point (in units of optical thickness) is 0.01 in the above solutions. A smaller value of 0.001 was also used, which had little effect on the accuracy of the solution (the result had less than 0.1% difference). It was an indication that the error caused by the angular quadrature was larger than that of distance quadrature, since increasing the number of grid points also didn't improve the accuracy.

Spectral Integration

Using S12, a 9 × 9 × 9 grid, and 0.01 as the first integration point, the spectral effect was examined by using 0.21 mole fraction of 1,000 K CO_2 at 1 atm within the cubic geometry. The walls were cold and black. The accuracy of spectral integration increased as more spectral points were used. In this study, the spectral integration incurred the largest error in the results. It was found that the total surface heat flux approached the analytical result using mean beam length theory as the number of spectral points used for spectral integration increased. In Figs. 3 and 5, the volume node (1, 1, 1) was at the coordinate of (1/18, 1/18, 1/18), volume node (5, 5, 5) at the coordinate of (1/2, 1/2, 1/2), surface node (1) at the coordinate of (1, 1/18, 1/18), and surface node (41) at the coordinate of (1, 1/2, 1/2). Eighty nonuniformly spaced spectral points used in a trapezoidal summation seemed to obtain fine resolution in the absorbing bands, and achieved convergence (Fig. 5). However, to reduce the total computational time, the spectral integration points were successively reduced which resulted in less than 1% error in the total quantities. The eliminated spectral points were chosen in order not to change the spectral profiles of the integrands, e.g., the points within $3.22 \leq \lambda \leq 4.03$ μm. For all the spectral calculations, 55 optimally selected spectral integration points were used. The locations of these points are shown in Fig. 1. The points were populated around the CO_2 absorbing bands.

The total surface heat flux on the wall was found to be $4.703 \cdot 10^4$ W with 80 spectral integration points and $4.713 \cdot 10^4$

W with 55 points, as compared to the $4.5 \cdot 10^4$ W using the Hottel's mean beam length theory and total emissivity chart.[4]

Results

The computation was performed on a Cray Y-MP/864 supercomputer. The most time-consuming part of the calculation was the YIX distance quadrature. This portion of the computation was not vectorized. It is believed that after modification of the code to take advantage of vectorization, an order of magnitude reduction in CPU time is possible. The one-dimensional problems were also run on a VAX 6400 computer in scalar mode, and the run time increased by a factor of 3.7 as compared to that on the Cray. Tables 2 and 3 show the CPU time for all the cases. In Tables 4–7, the surface flux and divergence of the radiative flux were all normalized with respect to the blackbody emissive power at 1000 K.

Three-Dimensional Homogeneous Problem

Radiative heat transfer was solved within the rectangular enclosure with cold and black boundaries, and the carbon particles were uniformly distributed. The participating medium had a mixture temperature of 1000 K, and a total pressure of 1 and 3 atm, and carbon particle concentrations of $2 \cdot 10^7$, $2 \cdot 10^8$, and $2 \cdot 10^9$ m^{-3}, $L = 5$ or 8 m as shown in Fig. 3 (a total of 12 cases).

The three-dimensional problems are computationally intensive. The magnitude of the first point of YIX quadrature also determined the accuracy of the integration. In the current

Table 2 Comparison of CPU time for the three-dimensional homogeneous medium cases under different conditions

Case number	Total pressure, atm	Carbon particles, m^{-3}	Length in y axis: L, m	CPU time, s
C1	1	$2 \cdot 10^7$	5	1317
C2	1	$2 \cdot 10^8$	5	2284
C3	1	$2 \cdot 10^9$	5	5267
C4	3	$2 \cdot 10^7$	5	1554
C5	3	$2 \cdot 10^8$	5	2365
C6	3	$2 \cdot 10^9$	5	4940
C7	1	$2 \cdot 10^7$	8	2056
C8	1	$2 \cdot 10^8$	8	3601
C9	1	$2 \cdot 10^9$	8	8140
C10	3	$2 \cdot 10^7$	8	2422
C11	3	$2 \cdot 10^8$	8	3699
C12	3	$2 \cdot 10^9$	8	7636

Table 3 Comparison of CPU time for the three-dimensional nonhomogeneous medium cases under different conditions

Case number	Total pressure, atm	Carbon particles, m^{-3}	T_0, K	CPU time, s
D1	1	$5 \cdot 10^7$	500	2,861
D2	1	$5 \cdot 10^7$	750	2,897
D3	1	$5 \cdot 10^8$	500	5,732
D4	1	$5 \cdot 10^8$	750	5,885
D5	3	$5 \cdot 10^7$	500	3,744
D6	3	$5 \cdot 10^7$	750	3,542
D7	3	$5 \cdot 10^8$	500	6,430
D8	3	$5 \cdot 10^8$	750	6,077
D9	1	$5 \cdot 10^7$	500	4,591
D10	1	$5 \cdot 10^7$	750	4,625
D11	1	$5 \cdot 10^8$	500	9,133
D12	1	$5 \cdot 10^8$	750	9,345
D13	3	$5 \cdot 10^7$	500	6,034
D14	3	$5 \cdot 10^7$	750	5,698
D15	3	$5 \cdot 10^8$	500	10,275
D16	3	$5 \cdot 10^8$	750	9,576

The total length in y dimension for cases D1–D8 is 5 m, and for cases D9–D16 is 8 m.

Table 4 Surface heat flux for the three-dimensional homogeneous medium cases at $y = 0$, and $z = H/2$

Case	$x/W = 0$	$x/W = \frac{1}{8}$	$x/W = \frac{1}{4}$	$x/W = \frac{3}{8}$	$x/W = \frac{4}{9}$
C1	0.1977	0.1970	0.1926	0.1770	0.1639
C2	0.4143	0.4113	0.3976	0.3546	0.3195
C3	0.9212	0.9131	0.8824	0.7927	0.7061
C4	0.2555	0.2545	0.2493	0.2305	0.2141
C5	0.4557	0.4526	0.4386	0.3945	0.3579
C6	0.9267	0.9190	0.8898	0.8034	0.7196
C7	0.2022	0.2013	0.1956	0.1797	0.1668
C8	0.4281	0.4247	0.4077	0.3634	0.3284
C9	0.9214	0.9132	0.8826	0.7928	0.7062
C10	0.2603	0.2592	0.2525	0.2333	0.2172
C11	0.4688	0.4653	0.4483	0.4029	0.3664
C12	0.9268	0.9191	0.8900	0.8035	0.7197

Table 5 Divergence of radiative heat flux for the three-dimensional homogeneous medium cases at $y = z = 0$

Case	$x/W = 0$	$x/W = \frac{1}{8}$	$x/W = \frac{1}{4}$	$x/W = \frac{3}{8}$	$x/W = \frac{4}{9}$
C1	0.1408	0.1441	0.1576	0.2252	0.3083
C2	0.4586	0.4643	0.4859	0.5729	0.6737
C3	0.2697	0.3363	0.5807	1.2660	1.9170
C4	0.1603	0.1655	0.1867	0.2772	0.3819
C5	0.4501	0.4578	0.4871	0.5981	0.7221
C6	0.2543	0.3184	0.5559	1.2370	1.8910
C7	0.1387	0.1419	0.1557	0.2237	0.3067
C8	0.4502	0.4560	0.4786	0.5670	0.6678
C9	0.2677	0.3344	0.5790	1.2650	1.9160
C10	0.1576	0.1629	0.1843	0.2754	0.3801
C11	0.4416	0.4494	0.4797	0.5922	0.7160
C12	0.2524	0.3166	0.5543	1.2360	1.8900

Table 6 Surface heat flux for the three-dimensional nonhomogeneous medium cases at $y = 0$ and $z = H/2$

Case	$x/W = 0$	$x/W = \frac{1}{8}$	$x/W = \frac{1}{4}$	$x/W = \frac{3}{8}$	$x/W = \frac{4}{9}$
D1	0.0299	0.0298	0.0255	0.0220	0.0201
D2	0.1602	0.1591	0.1371	0.1182	0.1076
D3	0.0727	0.0707	0.0617	0.0513	0.0450
D4	0.3948	0.3834	0.3356	0.2798	0.2459
D5	0.0340	0.0338	0.0291	0.0250	0.0228
D6	0.1790	0.1772	0.1534	0.1323	0.1205
D7	0.0728	0.0707	0.0617	0.0514	0.0451
D8	0.3954	0.3828	0.3354	0.2801	0.2466
D9	0.0321	0.0324	0.0277	0.0236	0.0215
D10	0.1714	0.1718	0.1482	0.1262	0.1145
D11	0.0765	0.0746	0.0648	0.0536	0.0467
D12	0.4146	0.4031	0.3516	0.2915	0.2546
D13	0.0364	0.0364	0.0313	0.0267	0.0243
D14	0.1904	0.1900	0.1644	0.1402	0.1274
D15	0.0765	0.0744	0.0646	0.0535	0.0467
D16	0.4143	0.4018	0.3509	0.2914	0.2550

Table 7 Divergence of radiative heat flux for the three-dimensional nonhomogeneous medium cases at $y = z = 0$

Case	$x/W = 0$	$x/W = \frac{1}{8}$	$x/W = \frac{1}{4}$	$x/W = \frac{3}{8}$	$x/W = \frac{4}{9}$
D1	0.8378	0.3587	0.1398	0.0386	0.0089
D2	3.8250	1.7840	0.7465	0.2214	0.0534
D3	3.1040	1.1950	0.3970	0.0615	−0.0262
D4	14.430	5.9020	2.1130	0.3944	−0.0910
D5	0.9287	0.3952	0.1542	0.0421	0.0087
D6	4.2180	1.9270	0.7997	0.2317	0.0494
D7	3.0540	1.1660	0.3872	0.0594	−0.0269
D8	14.260	5.7780	2.0580	0.3766	−0.0988
D9	0.8266	0.3502	0.1350	0.0369	0.0086
D10	3.7720	1.7430	0.7224	0.2120	0.0512
D11	3.0230	1.1360	0.3650	0.0507	−0.0280
D12	14.050	5.6250	1.9610	0.3424	−0.0993
D13	0.9136	0.3840	0.1479	0.0398	0.0082
D14	4.1500	1.8730	0.7689	0.2197	0.0469
D15	2.9730	1.1070	0.3552	0.0485	−0.0286
D16	13.890	5.5000	1.9050	0.3248	−0.1067

case, the integration had accuracy on the order of 10^{-3} which is much smaller than the error caused by spectral integration. In all calculations, no convergence difficulty was encountered. The CPU time depended on the optical thickness, i.e., it was longer in absorbing bands and shorter in nonabsorbing bands. Initially, the first integration point of optical distance = 0.01 for the YIX quadrature was used. However, it was found that the use of 0.015 with the S12 discrete ordinate set produced very little change in the results, but had nearly 30% reduction of the CPU time. The results of 0.015/S12 combination compared with those of 0.01/S16 combination, showed less than 0.1% difference in flux divergence and less than 1% difference in heat flux, but the time reduction was much more significant. Hereafter, the 0.015/S12 combination is used for all the three-dimensional calculations. For the cases with $L = 5$ m, a $9 \times 13 \times 9$ (in x-y-z sense) grid was used, and with $L = 8$ m, a $9 \times 21 \times 9$ grid was used.

Table 4 lists the normalized surface heat flux and Table 5 lists the divergences of normalized radiative flux for all cases at specified locations. Physically, the flux divergence can be represented as a heat source (positive divergence) or sink (negative divergence). At the central region of the enclosure, as the particle concentration increased from $2 \cdot 10^7$ to $2 \cdot 10^8$, then $2 \cdot 10^9$ m^{-3}, the divergence first increased then decreased. The heat flux within the medium also behaved similarly. This seemed to suggest that there was an optimum value of particle concentration which would promote the radiative heat transfer within the medium most effectively. However, the surface heat flux, as well as the divergence near the boundary, were always the largest at the highest particle concentration. The radiative heat loss to the cold boundary increased due to the large number of emissive particles and the temperature jump at the walls. At the highest particle concentration ($2 \cdot 10^9$ m^{-3}), the medium was acting more like a good radiative insulation and the divergence near the central regions was therefore reduced from that for a concentration of $2 \cdot 10^8$ m^{-3}. At large optical thickness, heat exchange occurs only near the boundaries. In each case, at the corners of the plane parallel to the coordinate axis, the flux divergence is the largest, especially at the six corners of the rectangle enclosure where the volume nodes had three surfaces in contact with cold walls. This simply reflected the fact that to maintain uniform temperature in the homogeneous media, a larger heat source was needed near the cold wall.

In all cases, the increase of pressure from 1 to 3 atm slightly increased the flux and divergence, except for the cases with $2 \cdot 10^9$ m^{-3} particle concentration. In the latter case, the heat flux within the medium and divergence were reduced, but the surface heat flux still had a small increase as pressure increased to 3 atm. The small reduction of flux and divergence at high pressure was due to the stronger absorption of CO_2 superimposed on the already large optical thickness medium which further inhibited the effectiveness of the particles on radiative transfer.

For the cases with $L = 8$ m, the region within $-2/21 < y/L < 2/21$ behaved as two-dimensional, i.e, the flux and divergence depended only on the x and z directions. Since the L is much larger than W and H in these cases, the result was expected.

Three-Dimensional Nonhomogeneous Problem

The geometry is the same as stated for the three-dimensional homogeneous problem. However, the boundaries are gray, diffusely reflecting and emitting, and have an emissivity of 0.7. The temperature of the mixture was specified by

$$T(x, y, z) = T_0 \left[\left(1 - \frac{2|x|}{W}\right)\left(1 - \frac{|2y|}{L}\right)\left(1 - \frac{2|z|}{H}\right) + 1 \right] \tag{20}$$

and the carbon particles had the following distribution:

$$N(x, z) = N_0 \left[3\left(1 - \frac{2|x|}{W}\right)\left(1 - \frac{2|z|}{H}\right) + 1 \right] \tag{21}$$

With $T_0 = 500$ and 750 K, $N_0 = 5 \cdot 10^7$ and $5 \cdot 10^8$ m^{-3} and a total pressure of 1 and 3 atm, the radiative transfer within the enclosure was solved (a total of 16 cases). Table 6 lists the surface heat flux normalized by 1000 K blackbody emissive power for all cases at specified locations. Table 7 lists the divergence of normalized radiative flux for all cases. Figures 6 and 7 show the divergence at the $y = \pm 6L/13$ and 0 planes for case D3.

In addition to the particle density and pressure variations, temperature effects were studied in the nonhomogeneous medium. Since the temperature was higher near the center of the enclosure, the variation of the flux divergence was contrary to the previous case of the homogeneous medium (compare Tables 5 and 7). The divergence at the center was always highest. In the region between the center and the boundaries, the divergence was the lowest for the cases with $N_0 = 5 \cdot 10^7$ m^{-3}. Although the boundaries were cold, they diffusely reflected part of the energy back to the medium. Hence, the divergence at the volume nodes near the boundaries was not the lowest. However, for the cases with $N_0 = 5 \cdot 10^8$ m^{-3}, except on the plane layers of the volume nodes next to the $z = \pm H/2$ boundaries, the divergence at the nodes next to the walls was the lowest, and sometimes negative near $y = z = 0$, $x = \pm W/2$. This may be attributed to the combined effect of strong scattering and nonuniform distribution of carbon particles [see Eq. (21)]. To maintain the prescribed temperature profile, heat needs to be removed from the region close to $y = z = 0$, $x = \pm W/2$, because these locations were where the largest temperature gradient existed and the influence from the hot center region was the strongest.

Under the same conditions, with N_0 increased from $5 \cdot 10^7$ to $5 \cdot 10^8$ m^{-3}, the divergence increased nearly by a factor of

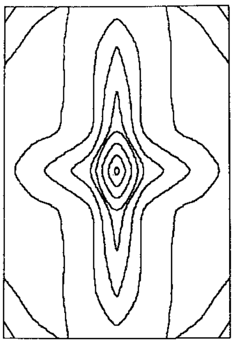

Fig. 6 Normalized flux divergence contour of the three-dimensional nonhomogeneous problem of case D3 at $y = \pm 6L/13$ m. The highest value is at the center.

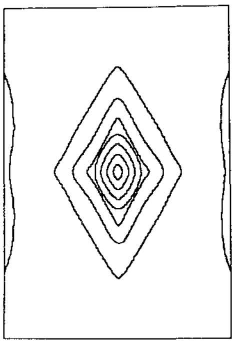

Fig. 7 Normalized flux divergence contour of the three-dimensional nonhomogeneous problem of case D3 at $y = 0$ m. The highest value is at the center and note the negative values at the left and right sides.

3, which indicated strong radiative transfer caused by the carbon particles. With other conditions unchanged and T_0 increased from 500 to 750 K, the divergence and flux increased by about 5–6 times (note that the blackbody emissive power at the center increased by a factor of five). While changing the pressure from 1 to 3 atm, there was a slightly increased flux and divergence. As previously shown for the homogeneous cases, the pressure effect was less significant than the other effects (particle density and temperature).

The approach to two-dimensional results observed in the homogeneous medium was not seen in the nonhomogeneous cases. This was due to the nonuniform distribution of carbon particles and temperature. In all cases, the surface heat flux was the highest at the center of the boundary surfaces because of the close proximity between the hot source and the boundary center.

Conclusions

Numerical solution of multidimensional radiative heat transfer integral equations involving a mixture of highly anisotropic scattering particles and a spectrally-dependent absorbing gas is presented. Results for the three-dimensional calculations are discussed. For a total pressure increase from 1 to 3 atm, the effect on the heat flux is insignificant, especially in the high particle density cases.

The nonhomogeneous cases show different distributions of the flux divergence but similar surface flux distribution. This is basically due to the nonuniform particle distribution and nonisothermal temperature distribution.

The present method of the YIX quadrature and discrete ordinates is shown to be able to solve complicated multidimensional homogeneous problems as well as nonhomogeneous problems without additional effort. The approach is proved to be flexible and accurate while the computational time can be further reduced by vectorization of the code.

References

[1] Tan, Z., "Radiative Heat Transfer in Multidimensional Emitting, Absorbing, and Anisotropic Scattering Media—Mathematical Formulation and Numerical Method," *Journal of Heat Transfer*, Vol. 111, No. 1, 1989, pp. 141–147.

[2] Lathrop, K. D., "Ray Effects in Discrete-Ordinates Equations," *Nuclear Science and Engineering*, Vol. 32, 1968, pp. 357–369.

[3] Tan, Z., and Howell, J. R., "A New Numerical Method for Radiation Heat Transfer in Nonhomogeneous Participating Media," *Journal of Thermophysics and Heat Transfer*, Vol. 4, No. 4, 1990, pp. 419–424.

[4] Siegel, R., and Howell, J. R., *Thermal Radiative Heat Transfer*, 3rd ed., McGraw-Hill, New York, 1993.

[5] Chu, C. M., and Churchill, S. W., "Representation of an Angular Distribution of Radiation Scattered by a Spherical Particle," *Journal of the Optical Society of America*, Vol. 45, 1955, pp. 958–962.

[6] Crosbie, A. L., and Davidson, G. W., "Dirac-Delta Function Approximations to the Scattering Phase Function," *Journal of Quantitative Spectroscopy & Radiative Transfer*, 1985, Vol. 33, No. 4, pp. 391–409.

[7] Menguc, M. P., and Viskanta, R., "Radiative Transfer in Three-Dimensional Rectangular Enclosures Containing Inhomogeneous, Anisotropically Scattering Media," *Journal of Quantitative Spectroscopy & Radiative Transfer*, Vol. 33, No. 6, 1985, pp. 533–549.

[8] Gradshteyn, I. S., and Ryzhick, I. M., *Table of Integrals, Series, and Products*, Academic Press, New York, 1980.

[9] Edwards, D. K., Glassen, L. K., Hausen, W. C., and Tuchscher, J. S., "Radiative Heat Transfer in Nonisothermal Nongray Gases," *Journal of Heat Transfer*, Vol. 89, No. 3, 1967, pp. 219–229.

[10] Edwards, D. K., "Molecular Gas Band Radiation," *Advances in Heat Transfer*, edited by T. F. Irvine, Jr., and J. P. Hartnett, Vol. 12, Academic Press, New York, 1976, pp. 115–193.

[11] Carlson, B. G., and Lathrop, K. D., "Transport Theory—The Method of Discrete-Ordinates," *Computing Methods in Reactor Physics*, edited by H. Greenspan, C. N. Kelber, and D. Okrent, Gordon and Breach, New York, 1968.

[12] Fiveland, W. A., "Three-Dimensional Radiative Heat-Transfer Solutions by the Discrete-Ordinates Method," *Journal of Thermophysics and Heat Transfer*, Vol. 2, No. 4, 1988, pp. 309–316.

[13] Tan, Z., "New Numerical Methods for Radiation Heat Transfer and Rarefied Gas Dynamics," Ph.D. Dissertation, Mechanical Engineering Dept., Univ. of Texas, Austin, TX, 1991.

[14] Larsen, M. E., "The Exchange Factor Method, an Alternative Zonal Formulation for Analysis of Radiating Enclosure Containing Participating Media," Ph.D. Dissertation, Mechanical Engineering Dept., Univ. of Texas, Austin, TX, 1983.

[15] Lathrop, K. D., and Carlson, B. G., "Discrete-Ordinates Angular Quadrature of the Neutron Transport Equation," Los Alamos Scientific Lab., Rept. LASL-3186, Los Alamos, NM, 1965.